# WO$_3$/TiO$_2$ nanocomposites: Salt–ultrasonic assisted hydrothermal synthesis and enhanced photocatalytic activity

Ximing Luo [a], Fangfang Liu [b], Xiaohui Li [b], Hongtao Gao [b,c],*, Guangjun Liu [c]

[a] School of Ocean Sciences, China University of Geosciences, Beijing 100083, PR China
[b] State Key Laboratory Base of Eco-chemical Engineering, Qingdao University of Science & Technology, Qingdao 266042, PR China
[c] Department of Chemistry and Chemical Engineering, Jining University, Qufu 273155, PR China

## ARTICLE INFO

## ABSTRACT

A series of WO$_3$/TiO$_2$ composite photocatalysts were fabricated *via* a facile salt–ultrasonic assisted hydrothermal process. The obtained samples were characterized by X-ray diffraction, scanning eletron microscopy, energy dispersive X-ray spectroscopy and UV–vis diffused reflectance spectroscopy. It was confirmed that anatase TiO$_2$ and monoclinic WO$_3$ coexisted in the composites. The photocatalytic activity of as-prepared WO$_3$/TiO$_2$ composites for degradation of Rhodamin B (RhB) under visible light irradiation was investigated. The results showed that WO$_3$/TiO$_2$ composites have a higher photocatalytic activity than those of pure TiO$_2$ and pure WO$_3$. First-principle calculations based on density functional theory were performed to explore the electronic structure and illustrate the photocatalytic mechanism of WO$_3$/TiO$_2$. The calculated energy gap was 2.53 eV, which was close to the experimental observation (2.58 eV). Due to the combination of WO$_3$/TiO$_2$, the photoinduced electrons and holes transfer between the WO$_3$ and TiO$_2$ in opposite directions, thus providing sufficient charge separation, which contributed to the photocatalytic activity enhancement.

© 2013 Elsevier Ltd. All rights reserved.

## 1. Introduction

Semiconductor photocatalysis has received much attention as a potential solution to the worldwide energy shortage and for counteracting environmental degradation [1–3]. Since Fujishima and Honda discovered the photo-electrochemical splitting of water on a TiO$_2$ electrode [4–6], intense research has been carried out on TiO$_2$ photocatalysis, which has been focused on understanding the fundamental principles, enhancing the photocatalytic efficiency, and expanding the scope of applications [7–9]. Due to its ability to decompose harmful organic pollutants completely, TiO$_2$ has been widely used for wastewater treatment, air purification, sterilization and environmental purification [10–13].

Unfortunately, TiO$_2$ is not ideal for all purposes and performs rather poorly in processes associated with solar photocatalysis. In principle, TiO$_2$ can utilize no more than 5% of the total solar energy impinging on the surface of the earth due to its wide band gap (3.0–3.2 eV) [14–17]. At the same time, the stimulated electron–hole on the TiO$_2$ surface can emerge easily, leading to the reduction of light catalytic efficiency [18,19]. It is still a challenge to develop high performance photocatalysts toward broader solar response. Many strategies have been used to modify the properties of TiO$_2$ and find other semiconductor photocatalysts to utilize solar energy efficiently. It has been reported that fabricating composites with CdS [20], SnO$_2$ [21], WO$_3$ [22], ZrO$_2$ [23], or CeO$_2$ [24], for example, is an effective method to broaden the spectral range of photoabsorption, promote charge separation and reduce the

---

* Corresponding author at: State Key Laboratory Base of Eco-chemical Engineering, Qingdao University of Science & Technology, Qingdao 266042, PR China. Tel.: +86 532 84022681; fax: +86 532 84023927.
  E-mail address: gaohongtao@gmail.com (H. Gao).

recombination rate. Nanostructure $WO_3$, as one of the n-type semiconductors with a band gap of 2.80 eV, has attracted much interest [25–27]. Since the photochromic process of $WO_3$ can be made completely reversible by exposing it to oxygen, it has been considered to be one of the most promising candidates for technological applications such as erasable optical storage devices, photocatalysts, electrochromic devices, and solar-energy devices [28–31]. $WO_3/TiO_2$ composites have been extensively investigated as energy storage photocatalysts, which can store the electrons generated by light irradiation and release them in the dark to participate in electron-mediated reactions [32].

In the present work, we reported a facile approach to synthesize $WO_3/TiO_2$ nanocomposites. The obtained samples were characterized by X-ray diffraction (XRD), scanning electron microscopy (SEM), energy dispersive X-ray spectroscopy (EDS) and UV–visible diffuse reflectance spectra (DRS). The photocatalytic activities of $WO_3/TiO_2$ composites were investigated on the degradation of Rhodamine B (RhB). First-principle calculations based on density functional theory (DFT) were adapted to explore the electronic properties and illustrate the photocatalytic mechanism of $WO_3/TiO_2$ composites. Due to the combination of $WO_3$ and $TiO_2$, the photoinduced electrons and holes transfer between the $WO_3$ and $TiO_2$ in opposite directions, thus providing sufficient charge separation, which contributed to the photocatalytic activity enhancement. The theoretical calculations could explain the experimental observation and present the electron transition route in photocatalytic reaction.

## 2. Experimental

### 2.1. Synthesis of $WO_3/TiO_2$

All chemicals were of analytical grade and used without further purification. A typical synthesis process for the preparation of $WO_3/TiO_2$ (molar ratio 1:1) nanocomposite oxides was as follows: $Ti(SO_4)_2$ (8 mmol) was first dissolved into 40 mL of $NaNO_3$ solution (2 M) under vigorous stirring, and then $Na_2WO_4 \cdot 2H_2O$ (8 mmol) was added. After further agitating for 30 min, the beaker filled with the solution was put into an ultrasonic cleaning device for 30 min in order to disperse fully and facilitate the completion of precipitate reaction. The solution was then migrated into a 50 mL Teflon-lined high-pressure reaction autoclave, and maintained at 150 °C for 12 h. Then the autoclave was allowed to cool to room temperature naturally, and white samples were collected, washed with redistilled water and absolute alcohol several times in proper sequence, and dried in an oven at 60 °C overnight. Subsequently, the samples were calcined at 550 °C for 2 h to gain the products.

### 2.2. Characterization

The crystalline phase of the powders evolved after calcination was examined by X-ray diffraction (XRD), which was carried out on a Bruker D8 advance X-ray diffractometer equipped with graphite monochromatized Cu Kα radiation ($\lambda = 1.54056$ Å) operated at 45 kV and 40 mA. The crystal size was calculated from X-ray line broadening applying the Scherrer equation

$$D = \frac{K\lambda}{\beta \cos\theta} \tag{1}$$

where $\lambda$ is the wavelength of the X-ray employed, $\beta$ is the full-width at half-maximum of the peak, $K$ (here $K=0.9$) is a constant, and $\theta$ is the Barge angle of the XRD peak. A scanning electron microscope JSM-6300 (JEOL Ltd., Japan) was used to investigate the surface morphology of the sample under the specified conditions of 20 keV, 16 mm working distance, and $5000 \times$ magnification. In addition, UV–vis diffuse spectra were measured at room temperature with a UV–vis spectrometer (TU-1901; Beijing Purkinje General Instrument Co., Ltd., China).

### 2.3. Measurement of photocatalytic activities

Photocatalytic experiments were conducted to decompose RhB in a photocatalyst aqueous suspension system, which were performed in an SGY-I photochemical reactor (Nanjing, Stonetech. EEC Ltd. Nanjing, China). A quartz cylinder (50 mm × 450 mm) was placed inside the reactor and a 300 W Xenon lamp with a 400 nm cutoff filter was used as the visible light irradiation source. For each condition, $WO_3/TiO_2$ samples (0.200 g) were added into 200 mL of RhB aqueous solution ($10^{-5}$ mol L$^{-1}$). Prior to irradiation, the solutions containing catalysts were stirred in the dark for 30 min to ensure the establishment of an adsorption–desorption equilibrium between photocatalyst powders and RhB. The photocatalytic experiment was repeated under the identical reaction conditions to confirm the reproducibility. At given time intervals, 5 mL of aqueous suspension was taken from the quartz cylinder after specific intervals, centrifuged and filtered through a 0.45 μm millipore filter to monitor the degradation of RhB dye. A UV spectrophotometer (TU-1901, Beijing Purkinje General Instrument Co., Ltd., China) was used to monitor changes in the spectral intensity distribution of RhB.

## 3. Results and discussion

### 3.1. XRD analysis

The crystal structure of the product was characterized by X-ray diffraction (XRD) measurement. The XRD pattern for $WO_3/TiO_2$ composite (molar ratio 1:1) prepared at 550 °C is depicted in Fig. 1. It presented that there were representative of the respective crystal phases for both anatase $TiO_2$ and monoclinic $WO_3$. The peaks at $2\theta=25.4°$ and 48.2° are representatives of the (101) and (200) planes of the anatase crystal phase of $TiO_2$ respectively (JCPDS ♯ 21-1272). Peaks at $2\theta=23.1°$, 23. 6°, 24.1°, 28.8°, 33.2°, 34.1°, 49.9°, 54.3° and 55.1° are indicative of the (002), (020), (200), (112), (022), (220), (140), (202) and (124) crystal planes of the monoclinic phase of $WO_3$ respectively (JCPDS ♯ 43-1035), which can be seen in Fig. 1. It was confirmed that anatase $TiO_2$ and monoclinic $WO_3$ coexisted in the composites. The higher number of $WO_3$ peaks is an indication that the growth of $WO_3$ has a wider range of crystal growth velocities.
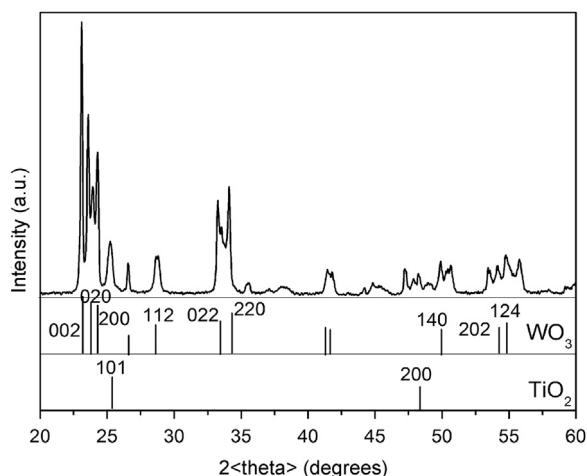
**Fig. 1** XRD image of as-synthesized $WO_3/TiO_2$ (molar ratio 1:1).
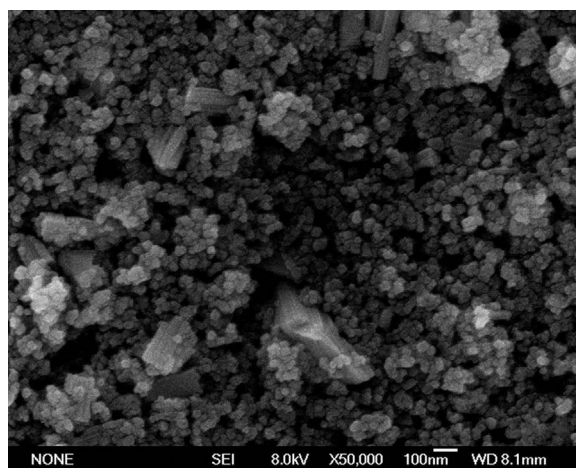


**Fig. 2.** SEM image of as-synthesized $WO_3/TiO_2$ (molar ratio 1:1).

### 3.2. SEM analysis

Fig. 2 exhibits the SEM image of $WO_3/TiO_2$ composite (molar ratio 1:1) calcined at 550 °C. The sample presented three morphologies: rough particles, globular crystalline particles and some irregular bodies. Further observation indicated the morphology of specimen, whose globular crystalline particles were uniformly distributed. It demonstrated $TiO_2$ coupled with amorphous and crystalline $WO_3$. A larger scale SEM image of $WO_3/TiO_2$ powders surface revealed that their structures appeared to be composed of nanoparticles, whose particle sizes were approximately 20–30 nm. Due to this characteristic of textured structure, the surface area of the products was enhanced significantly. This textured surface may be beneficial for enhancing the absorption of target substance, which would increase the photocatalytic performance of the samples.

### 3.3. EDS analysis

EDS analysis was carried out to determine the average weight ratio of $WO_3/TiO_2$ powders. The EDS image of $WO_3/TiO_2$ (molar ratio 1:1) sintered at 550 °C is illustrated in Fig. 3. From the EDS spectrum of $WO_3/TiO_2$ composite, the peaks of W, Ti and O could be clearly seen, indicating that Ti, W and O elements were contained in the product. According to further analysis, the atomic quantity ratio of W:Ti is about 1.06:1, which is very close to its stoichiometry of 1:1. It was confirmed that the molar ratio of anatase $TiO_2$ to monoclinic $WO_3$, coexisted in the composites, was 1:1.

### 3.4. DRS analysis

The optical absorption property of a semiconductor is related to the energy band structure, which is a key factor in evaluating the efficiency of light usage. The optical absorption edge and the energy gap can be calculated *via* UV–vis absorption spectrum. The UV–vis DRS for $WO_3/TiO_2$ composites with different molar ratios are presented in Fig. 4. It indicated that the as-prepared $WO_3/TiO_2$ photocatalysts
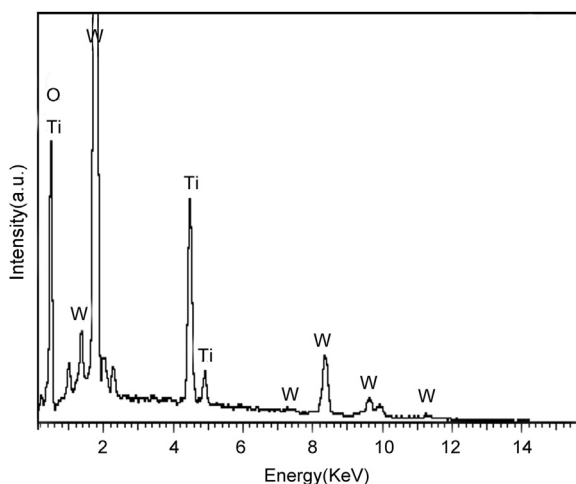


**Fig. 3.** EDS of $WO_3/TiO_2$ (molar ratio 1:1).
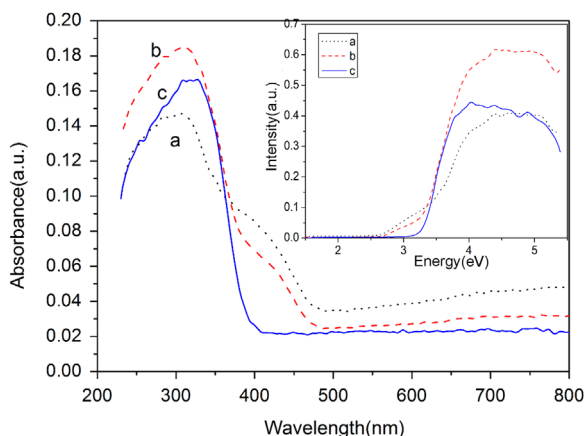


**Fig. 4.** Typical DRS of the $WO_3/TiO_2$ composites with different molar ratios: (a) 1:1, (b) 2:1, and (c) 1:2, insets are curves of $(\alpha h\nu)^{1/2}$ versus photon energy $(h\nu)$, from which the width of energy gap can be figured out by linear fitting of the absorption edge.
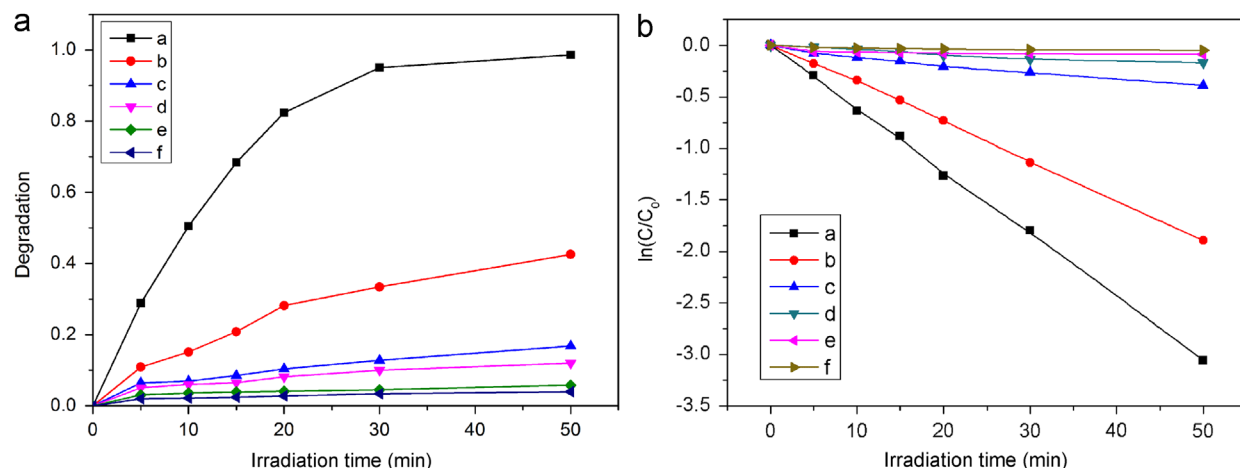
**Fig. 5.** (a) Photocatalytic degradation of RhB of the WO$_3$/TiO$_2$ composites with different molar ratios: (a) 1:1, (b) 2:1, (c) 1:2, (d) 1:0 (e) 0:1, and (f) blank (without photocatalyst). (b) Kinetic linear simulation curves of RhB photocatalytic degradation with the WO$_3$/TiO$_2$ products: (a) 1:1, (b) 2:1, (c) 1:2, (d) 1:0 (e) 0:1, and (f) RhB.

exhibited strong photoabsorption in both ultraviolet and visible light area. The absorption edge can be obtained by the perpendicular to the abscissa axis from the point of intersection of the two tangent lines from the absorption spectrum. As could be seen in Fig. 4, WO$_3$/TiO$_2$ composites with different molar ratios (1:1, 2:1 and 1:2) had absorption edges at about 480 nm, 475 nm and 398 nm, which are all in the visible region (390–750 nm), and the absorption edges have shifted to long wavelength. This is contrary to energy gap. The $E_g$ of the WO$_3$/TiO$_2$ composite semiconductor can be obtained using the equation (Eq. 2) [33]:

$$\alpha h\nu = A(h\nu - E_g)^{n/2} \qquad (2)$$

where $\alpha$, $h\nu$, $E_g$, and $A$ are absorption coefficient, light frequency, energy gap, and a constant, respectively. Assuming that the absorption coefficient $\alpha$ is proportional to the Kubelka–Munk function $F(R)$, the $E_g$ can be obtained from the plot of $[F(R)h\nu]^{1/n}$ versus $h\nu$, by extrapolation of the linear part near the onset of the absorption edge to intersect the energy axis. The corresponding energy gaps were 2.58 eV, 2.61 eV and 3.12 eV. The $E_g$ of the WO$_3$/TiO$_2$ composites was smaller than that of pure TiO$_2$ (3.2 eV). And the band gap for WO$_3$/TiO$_2$ (1:1) sample was the smallest (2.58 eV). It indicated that the photocatalyst WO$_3$/TiO$_2$ could exhibit photocatalytic activity under solar light irradiation.

### 3.5. Photocatalytic activity

The photocatalytic activities of catalysts were examined by measuring the degradation of RhB under visible light irradiation at room temperature. Fig. 5a shows the typical experimental results from photocatalytic degradation of RhB. It indicated that there were obvious photocatalytic activities under irradiation for all the as-prepared samples. As shown in Fig. 5a, the degradation of RhB was extremely slow without catalyst under visible light illumination. The degradation percentage of RhB is ca. 4% after irradiating for about 50 min. Thus the photolysis effect on the degradation of RhB could be negligible. There were evidently photocatalytic activities under visible-light irradiation for WO$_3$/TiO$_2$

composites. After being irradiating for 50 min, the degradation percentages of RhB for the catalysts with molar ratio 1:1, 2:1 and 1:2 respectively were 100%, 43% and 18% under visible light irradiation, while pure WO$_3$ (1:0) and pure TiO$_2$ (0:1) residues were 15% and 7% after 50 min visible light irradiation. So the photocatalytic activity of WO$_3$/TiO$_2$ (1:1, 2:1 and 1:2) nanocomposites was better than those of pure WO$_3$ and pure TiO$_2$. In comparison, WO$_3$/TiO$_2$ with molar ratio 1:1 nanostructures exhibited an obvious enhancement in photocatalytic performance.

Linearized kinetic data curves for RhB photocatalytic degradation with the WO$_3$/TiO$_2$ samples are presented in Fig. 5b. It is clear that the curve with $\ln(C/C_0)$ as ordinate and irradiation time as abscissa is close to linear, which indicates that photocatalytic degradation of RhB using the samples follows first-order reaction kinetics. The values of reaction rates $k$ for WO$_3$/TiO$_2$ (1:1), WO$_3$/TiO$_2$ (2:1), WO$_3$/TiO$_2$ (1:2), pure WO$_3$, pure TiO$_2$ and RhB samples were 0.0265, 0.0166, 0.0032, 0.0016, 0.0005 and 0.0004 min$^{-1}$, respectively, indicating favorable photocatalytic performance of the WO$_3$/TiO$_2$ photocatalyst. And the photocatalytic activity of the WO$_3$/TiO$_2$ (1:1) was the best.

### 3.6. Theoretical analysis

#### 3.6.1. Calculation models and methods

In order to explain the experimental observations, first-principle calculations based on density functional theory (DFT) were performed to probe the electronic properties of WO$_3$/TiO$_2$ composite in our work. The crystal structure of WO$_3$/TiO$_2$ nanocomposite was modeled by layers of anatase TiO$_2$ and monoclinic WO$_3$ with different thicknesses, which is presented in Fig. 6. In each calculation, stoichiometric slab models ($1 \times 1$) were used, consisting of 16 atomic layers and a total of 16 Ti atoms, 16 W atoms, and 80 O atoms for a unit cell. The anatase TiO$_2$ component is terminated by a twofold O atom and the monoclinic WO$_3$ component is terminated by one threefold W atom. The top tri-layer of atom is allowed to relax and all other layers are held fixed. In the case of layers, the vacuum thickness is 3 Å.

The calculations in our work have been carried out using the well tested CASTEP [34,35]. The general gradient approximation (GGA) with PW91 functional and ultra-soft pseudo-potentials was used to describe the exchange-correlation effects and electron–ion interactions, respectively. Structural optimization was performed with the Brillouin zone sampling being limited to the Γ point. O (2s2 2p4), W (5s2 5p6 5d4 6s2) and Ti (3d2 4s2) electrons were considered as valence states, while the remaining electrons were kept frozen as core states. The cutoff energy for the plane-wave basis was set as 340 eV. The Pulay density hybrid method was used in energy calculations; convergence threshold for self-consistent field was set to $1.0 \times 10^{-6}$ eV/atom. The $k$-point sampling of the Brillouin zone was set to $5 \times 7 \times 1$. The BFGS algorithm has been used for geometry optimizations and the atomic relaxation was carried out until all components of the residual forces were less than 0.03 eV/Å. In calculations, the geometry models of hetero-structures were optimized firstly, and then their electronic structures and optical properties were calculated. All the calculations were performed in the reciprocal space.

### 3.6.2. Electronic structure analysis

The electronic structure and the energy gap ($E_g$) play a crucial role in determining the photocatalytic activity of the semiconductor. The band structure and the projected density of states (PDOS) of $WO_3/TiO_2$ (1:1) nanocomposites are presented in Fig. 7a and b, respectively. The PDOS revealed that the bottom of conduction bands (CB) was mostly composed of W 5d states, and the top of valence bands (VB) was dominated by O 2p and Ti 3d states. It is shown in Fig. 8a that minimum gap between the valence band maximum (VBM) and the conduction band minimum (CBM) was 2.53 eV, which was corrected using a scissors operator [36]. It is consistent with our experimental observation and is lower than that of both monoclinic $WO_3$ (2.80 eV) and anatase $TiO_2$ (3.20 eV). When it was exposed under irradiation, the generation of electron–hole pairs were easier than both that of monoclinic $WO_3$ and
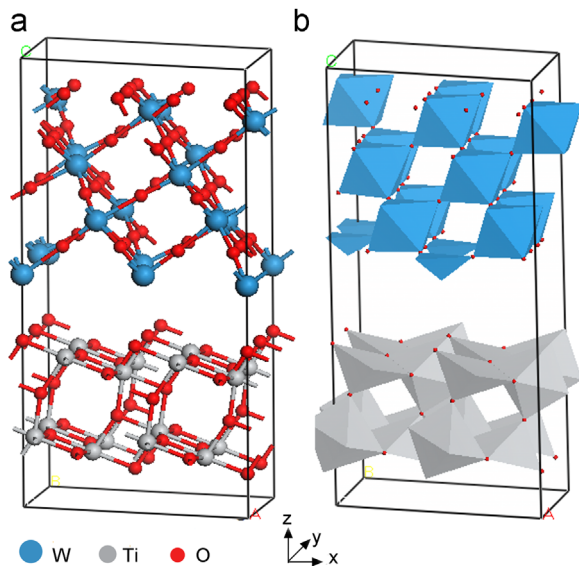
**Fig. 6.** The crystal structure of $WO_3/TiO_2$ nanocomposite. (a) The supercell model. (b) The corresponding polyhedron structure of $WO_3$ monoclinic are presented above and $TiO_2$ anatase is presented below.
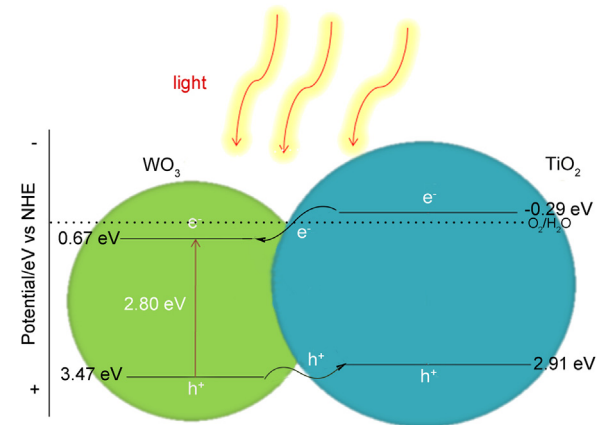
**Fig. 8.** Schematic describes the photocatalytic mechanism in the visible light for $WO_3/TiO_2$ system.
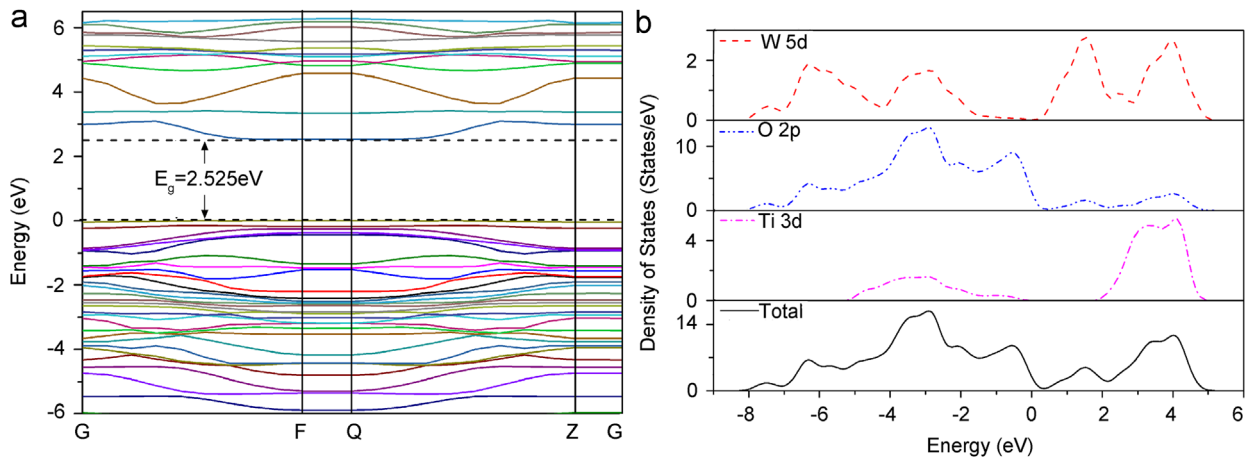
**Fig. 7.** The calculated energy band structure and PDOS for $WO_3/TiO_2$ nanocomposites with proper correction: (a) energy band structure, and (b) PDOS.

that of anatase $TiO_2$, which could account for the optical absorption edge shift toward lower energies (in the visible region). It can explain the transition illustrated in Fig. 8.

### 3.7. Photocatalytic mechanism

The energy edge positions of $WO_3$ and $TiO_2$ play a key role in determining the migration of charge carriers. So, it is significant to clarify the relative potential levels of their band edges. The conduction band edge of a semiconductor ($pH_{zpc}$) can be gained from the following equation:

$$E_{CB} = X - E_0 - 0.5E_g \qquad (3)$$

where $E_{CB}$ indicates the conduction band edge potential level of the semiconductor at the point of zero charge; $X$ is the geometric mean of the absolute electro-negativity of the component atoms; $E_0$ is the energy of free electrons on the hydrogen scale ($E_0 = -4.5$ eV for a normal hydrogen electrode (NHE)); and $E_g$ is the energy gap of the semiconductor. The predicted band edge potential levels of $WO_3$ and $TiO_2$ according to Eq. (3) are shown in Fig. 8. It can be seen in Fig. 8 that some of the photoexcited electrons transferred from the conduction band of $TiO_2$ to the conduction band of $WO_3$ due to more negative potential of $TiO_2$ conduction band. Similarly, photoinduced holes moved to the valence band of $TiO_2$. The photoinduced electrons and holes transfer between $WO_3/TiO_2$ in opposite directions, thus limiting recombination of the photogenerated species and providing sufficient charge separation, which contributed to the photocatalytic activity enhancement.

### 4. Conclusions

In summary, a series of $WO_3/TiO_2$ composites were prepared via a facile salt–ultrasonic assisted hydrothermal synthesis in mild condition. The products were characterized by XRD, SEM, EDS, and DRS. The experimental photocatalytic degradation of RhB observations indicated that the as-prepared $WO_3/TiO_2$ composites photocatalysts exhibited powerful photocatalytic performance under visible light irradiation. First-principle calculations were performed to illustrate the photocatalytic mechanism of $WO_3/TiO_2$ nanocomposites. The calculated energy gap was 2.53 eV, which is very close to the experimental observation 2.58 eV. The electron transition was more facile than that of both monoclinic $WO_3$ and anatase $TiO_2$, consistent with photoactivity in visible region. Due to the combination of $WO_3/TiO_2$, photoinduced electrons and holes transfer between the $WO_3$ and $TiO_2$ in opposite directions, providing sufficient charge separation, which contributed to the photocatalytic activity enhancement. Our approach provides an efficient route to improved visible-light-driven photocatalysts as well as promising materials for use in solar cells, related nanodevices, and other applications.

### Acknowledgments

### References

[1] Y.P. Xie, G. Liu, L.C. Yin, H.M. Cheng, Journal of Materials Chemistry (2012)6551–6746.
[2] M.C. Yin, Z.S. Li, J.H. Kou, Z.G. Zou, Environmental Science and Technology 43 (2009) 8361–8366.
[3] S.K. Cushing, J.T. Li, F.K. Meng, T.R. Senty, S. Savan, M.J. Zhi, M. Li, A.D. Bristow, N.Q. Wu, Journal of the American Chemical Society 134 (2012) 15033–15041.
[4] W. Smith, A. Wolcott, R.C. Fitzmorris, J. Zhang, Y.P. Zhao, Journal of Materials Chemistry 21 (2011) 10792–10800.
[5] A. Fujishima, K. Honda, Nature 238 (1972) 37.
[6] I. Paramasivam, Y.C. Nah, C. Das, N.K. Shrestha, P. Schmuki, Chemistry—A European Journal 16 (2010) 8993–8997.
[7] D.N. Ke, H.J. Liu, T.Y. Peng, X. Liu, K. Dai, Materials Letters 62 (2008) 447–450.
[8] F. Meng, J. Li, Z. Hong, M. Zhi, A. Sakla, C. Xiang, N. Wu, Catalysis Today 199 (2013) 48–52.
[9] S.Y. Chai, Y.J. Kim, W.I. Lee, Journal of Electroceramics 17 (2006) 909–912.
[10] S.G. Meng, D.Z. Li, M. Sun, W.J. Li, J.X. Wang, J. Chen, X.Z. Fu, G.C. Xiao, Catalysis Communications 12 (2011) 972–975.
[11] J.H. Sun, Y.K. Wang, R.X. Sun, S.Y. Dong, Materials Chemistry and Physics 115 (2009) 303–308.
[12] S.A.K. Leghari, S. Sajjad, F. Chen, J.L. Zhang, Chemical Engineering Journal 166 (2011) 906–915.
[13] L.S. Zhang, K.H. Wong, H.Y. Yip, C. Hu, J.C. Yu, C.Y. Chan, P.K. Wong, Environmental Science and Technology 44 (2010) 1392–1398.
[14] Y.D. Lu, J.J. Xu, Y. Liu, B.H. Liu, C.H. Xu, D.Y. Zhao, J.L. Kong, Chemical Communications (2006) 785–787.
[15] H. Tong, S. Ouyang, Y. Bi, N. Umezawa, M. Oshikiri, J.H. Ye, Advanced Materials 24 (2012) 229–251.
[16] F.K. Meng, Z.L. Hong, J. Arndt, M. Li, M.J. Zhi, F. Yang, N.Q. Wu, Nano Research 5 (3) (2012) 213–221.
[17] D. Su, J.Y. Wang, Y.P. Tang, C. Liu, L.F. Liu, X.J. Han, Chemical Communications 47 (2011) 4231–4233.
[18] C.F. Lin, C.H. Wu, Z. Nan, Journal of Hazardous Materials 154 (2008) 1033–1039.
[19] C.X. Feng, S.Z. Wang, B.Y. Geng, Nanoscale 3 (2011) 3695–3699.
[20] W. Zhang, Y.B. Wang, Z. Wang, Z.Y. Zhong, R. Xu, Chemical Communications 46 (2010) 7631–7633.
[21] M. Fujishima, Q.L. Jin, H. Yamamoto, H. Tada, M. Nolan, Physical Chemistry Chemical Physics 14 (2012) 705–711.
[22] R.M. Mohamed, D.L. McKinney, W.M. Sigmund, Materials Science and Engineering R 73 (2012) 1–13.
[23] X.F. Chen, X.C. Wang, X.Z. Fu, Energy and Environmental Science 2 (2009) 872–877.
[24] Y.T. Li, L. Chen, Y.L. Guo, X.G. Sun, Y. Wei, Chemical Engineering Journal 181 (2012) 734–739.
[25] T.Y. Ma, Z.Y. Yuan, J.L. Cao, European Journal of Inorganic Chemistry (2010) 716–724.
[26] X.H. Zhang, X.H. Lu, Y.Q. Shen, J.B. Han, L.Y. Yuan, L. Gong, Z. Xu, X.D. Bai, M. Wei, Y.X. Tong, Y.H. Gao, J. Chen, J. Zhou, Z.L. Wang, Chemical Communications 47 (2011) 5804–5806.
[27] K. Maeda, M. Higashi, D.L. Lu, R. Abe, K. Domen, Journal of the American Chemical Society 132 (2010) 5858–5868.
[28] J.J. Guo, Y. Li, S.M. Zhu, Z.X. Chen, Q.L. Liu, D. Zhang, RSC Advances 2 (2012) 1356–1363.
[29] A. Ponzoni, E. Comini, G. Sberveglieri, J. Zhou, S.Z. Deng, N.S. Xu, Y. Ding, Z.L. Wang, Applied Physics Letters 88 (2006) 203101–203103.
[30] J. Li, F. Meng, S. Suri, W. Ding, F. Huang, N. Wu, Chemical Communications 48 (2012) 8213–8215.
[31] T. He, Y. Ma, Y.A. Cao, X.L. Hu, H.M. Liu, G.J. Zhang, W.S. Yang, J.N. Yao, Journal of Physical Chemistry B 106 (2002) 12670–12676.
[32] D.M. Huang, S.H. Wan, L.P. Wang, Q.J. Xue, Surface and Interface Analysis 43 (2011) 1064–1068.
[33] S.Y. Wang, B.B. Huang, Z.Y. Wang, Y.Y. Liu, W. Wei, X.Y. Qin, X.Y. Zhang, Y. Dai, Dalton Transactions 40 (2011) 12670–12675.
[34] R. Asahi, Y. Taga, W. Mannstadt, A.J. Freeman, Physical Review B 61 (2000) 7459–7465.
[35] Z.H. Levine, D.C. Allan, Physical Review Letters 63 (1989) 1719–1722.
[36] K.S. Yang, Y. Dai, B.B. Huang, M.H. Whangbo, Chemistry of Materials 20 (2008) 6528–6534.